

ABSTRACT

27 High-resolution three-dimensional (3D) wind field data are critical for a wide range of
28 applications, including wind energy assessment, low-altitude aviation, air quality modeling, and
29 extreme weather forecasting. Although ERA5 reanalysis remains widely used, its relatively coarse
30 spatial resolution (~31 km) limits its ability to capture local-scale atmospheric processes. To
31 address this, this study develops an hourly 3D dynamic wind field dataset with 1 km horizontal
32 resolution covering the Yangtze River Delta (YRD) region during the summer months (June–
33 August) from 2021 to 2023, namely YRD1km, generated through advanced dynamical
34 downscaling of ERA5 using a customized Weather Research and Forecasting (WRF) model
35 configuration. The methodology integrates multi-source observational nudging with high-
36 resolution land use parameterization to enhance near-surface wind accuracy and terrain-induced
37 flow representation, particularly in urban clusters and mountainous areas. Validation against
38 ground-based observations confirms the superior performance of YRD1km over ERA5 for hourly
39 10-m wind components, with Mean Absolute Error (MAE) reduced by 21.61% for U and 26.04%
40 for V, Root Mean Square Error (RMSE) reduced by 18.30% for U and 22.63% for V, and Nash–
41 Sutcliffe Efficiency (NSE) improved by 33.27% and 40.13%, respectively. On a daily mean basis,
42 both MAE and RMSE are reduced to below 0.5 m/s, and NSE reaches approximately 0.88.
43 Spatially, YRD1km captures finer spatial wind speed gradients and localized terrain-induced
44 circulations that are not captured by ERA5. Temporally, consistent accuracy improvements with
45 approximately 20% lower hourly error variability are seen when compared to ERA5. Vertically,
46 42.18% accuracy gains are observed in the near-surface layer when compared with radiosonde
47 profiles. Moreover, convective case analyses indicate that YRD1km captures vertically coherent
48 wind structures across multiple tropospheric levels that are closely linked to the initiation and

49 maintenance of deep convection, highlighting its diagnostic advantage in high-impact weather
50 events. Overall, the YRD1km 3D wind field dataset and its integrated methodological framework
51 provide a robust foundation for regional meteorological applications, including high-resolution
52 AI-based forecasting, renewable energy planning, and weather risk management in rapidly
53 developing regions such as the YRD. The YRD1km 3D wind field dataset is available at
54 <https://doi.org/10.57760/sciencedb.23752> (Zhang et al., 2025).

55 **Key words:** 3D wind field dataset; dynamical downscaling; multi-source observational
56 nudging; high-resolution land use; Yangtze River Delta

57

58 **1. Introduction**

59 Accurate characterization of three-dimensional (3D) wind fields with high spatiotemporal
60 resolution is fundamental to modern meteorological services, wind energy development, and the
61 safe operation of low-altitude economy. Although widely used ERA5 atmospheric reanalysis
62 datasets are capable of providing wind field variables that exhibit temporal continuity and physical
63 consistency, their relatively coarse spatial resolution limits the capability to resolve regional-scale
64 wind field features (Hu et al., 2023; Jung and Schindler, 2022), particularly in areas with complex
65 terrain and intense urbanization (Molina et al., 2021).

66 The Yangtze River Delta (YRD), as one of the most intensely urbanized regions in China,
67 exhibits evident spatiotemporal heterogeneity in local wind fields due to the combined effects of
68 sea-land thermal contrasts, urban heat island effects, and boundary layer turbulence (Zhang et al.,
69 2010). This presents significant challenges for precise wind energy resource assessment, urban
70 ventilation capacity diagnosis, and early warning of wind storm events. To address these
71 challenges, spatial downscaling of coarse-resolution reanalysis datasets has become a promising

72 strategy for improving regional wind field reanalysis and supporting fine-scale applications (Boé
73 et al., 2007; Tang et al., 2016; Zhang et al., 2020).

74 Spatial downscaling techniques primarily include statistical downscaling and dynamical
75 downscaling approaches. Statistical downscaling establishes statistical relationships between
76 coarse-resolution meteorological variables and local observational data (Dayon et al., 2015;
77 Tareghian and Rasmussen, 2013), enabling the acquisition of high-resolution wind field
78 information at relatively low computational costs (Zamo et al., 2016). However, such methods
79 often overlook the physical constraints among meteorological variables. In recent years, deep
80 learning has been increasingly applied to enhance the accuracy of statistical downscaling of wind
81 fields (Dujardin and Lehning, 2022; Dupuy et al., 2023; Höhle et al., 2020; Lian et al., 2024; Liu
82 et al., 2024a; Zhang and Li, 2021). Nevertheless, incorporating physical consistency into deep
83 learning frameworks remains a significant challenge (Sun et al., 2024). In contrast, dynamical
84 downscaling employs the fundamental equations governing the atmospheric dynamics to explicitly
85 resolve physical processes, thereby reconstructing regional weather systems at high resolutions
86 (Tang et al., 2016). Its effectiveness has been demonstrated in various applications (Bao et al.,
87 2015; Liu et al., 2024b; Xu et al., 2021). Horvath et al. (2012) applied the Weather Research and
88 Forecasting (WRF) model with sub-kilometer grid spacing over mountainous regions of Nevada
89 and showed that dynamical downscaling significantly improved the representation of near-surface
90 wind speed and variability compared to coarser reanalysis products. Notably, when combined with
91 nudging techniques, the model's responsiveness to the actual atmospheric state is further enhanced
92 (Harkey and Holloway, 2013; Lo et al., 2008).

93 Nudging, also known as Newtonian relaxation, is a data assimilation method that introduces
94 forcing terms into numerical model equations to incrementally adjust model variables toward

95 observations or analysis fields (Hoke and Anthes, 1976). Compared with variational assimilation
96 methods, nudging does not require the construction of an adjoint model or the estimation of
97 background error covariance matrices. As a result, it offers a simpler implementation and lower
98 computational cost (Daescu and Langland, 2013; Lei and Hacker, 2015). Research has
99 demonstrated that this method has been successfully applied in the construction of several high-
100 resolution reanalysis datasets. For example, the MERIDA HRES (4 km resolution, hourly) (Viterbo
101 et al., 2024) and the BAYWRF (1.5 km resolution, daily) (Collier and Mölg, 2020) datasets both
102 employ the WRF model to perform dynamical downscaling on ERA5 reanalysis data. By
103 integrating nudging techniques, these datasets have reconstructed local wind field characteristics
104 for Italy and the Bavarian region of Germany, respectively. Although dynamical downscaling
105 demands substantial computational resources, advancements in regional model structures and
106 high-performance computing technologies are expected to greatly improve its feasibility for
107 regional complex terrain studies and non-climate research applications (Gutowski et al., 2020;
108 Yuan et al., 2024).

109 Furthermore, accurate representation of land surface parameters is another critical factor
110 influencing the performance of wind field dynamical downscaling. In recent years, high-resolution
111 land use data have been increasingly incorporated into wind field modeling to optimize surface
112 parameterization (De Bode et al., 2023; Fu et al., 2020; Santos-Alamillos et al., 2015). The updated
113 land use datasets enable more precise characterization of various land surface features such as
114 urban areas, mountainous regions, and water bodies, which improve simulation of terrain-induced
115 flows and boundary layer processes, particularly in complex terrain regions (Golzio et al., 2021;
116 Siewert and Kroszczynski, 2023).

117 In summary, this study presents the development of a 1-km hourly 3D dynamic wind field
118 dataset over the YRD region (YRD1km), covering the period of the summer months (June to
119 August) from 2021 to 2023. The YRD1km dataset is generated by applying a state-of-the-art
120 dynamical downscaling technique to the ERA5 reanalysis data, integrating multi-source
121 observational nudging, and updating land surface information with high-resolution ESA
122 WorldCover 2020 (EWC2020) land use data. The resulting dataset provides enhanced accuracy in
123 simulating near-surface winds and tropospheric dynamic structures, particularly in urban and
124 mountainous areas where wind variability is often high.

125 This study evaluates the performance of YRD1km relative to ERA5, with a focus on both
126 horizontal and vertical wind field accuracy. It also assesses the effectiveness of an integrated
127 methodology that combines dynamical downscaling, observational nudging, and updated land use
128 data in improving wind field simulations over regions with complex land surface characteristics
129 and atmospheric variability. The findings highlight the potential of YRD1km to support a wide
130 range of applications, such as high-resolution diagnostic analyses of regional wind fields,
131 renewable energy planning, air quality modeling, and urban environmental management in rapidly
132 urbanizing areas.

133 **2. Data**

134 **2.1 ERA5 Reanalysis Data**

135 The ERA5 reanalysis dataset (Hersbach et al., 2020), developed by the European Centre for
136 Medium-Range Weather Forecasts (ECMWF), integrates global multi-source observations
137 through 4D-Var data assimilation(<https://doi.org/10.24381/cds.bd0915c6>). It provides three-
138 dimensional hourly atmospheric variables (e.g., temperature, humidity, wind fields, and pressure)
139 with a horizontal resolution of $0.25^{\circ} \times 0.25^{\circ}$ (about 31km), serving as a widely adopted benchmark

140 in meteorological research. In this study, ERA5 supplies initial and boundary conditions for the
141 WRF model dynamical downscaling. Additionally, ERA5 serves as a baseline dataset for
142 comparative validation of YRD1km performance enhancements.

143 **2.2 Surface and Upper Air Weather Observations**

144 This study assimilates two observational datasets: (1) the NCEP ADP Global Upper Air and
145 Surface Weather Observations (<https://doi.org/10.5065/Z83F-N512>), comprising global terrestrial
146 stations, ocean buoys, ships, radiosondes, aircraft reports, and ASCAT satellite-derived winds from
147 the Global Telecommunication System (GTS), and (2) hourly data from Automatic Weather
148 Stations (AWS) operated by the China Meteorological Administration (CMA) (<http://data.cma.cn/>).
149 The spatial distributions of the two observational datasets over the YRD are illustrated in Figure
150 1a. The NCEP ADP dataset provides three-dimensional conventional meteorological
151 measurements from multiple observational platforms. As a complement to the NCEP ADP dataset,
152 the CMA AWS network delivers high-density surface observations across China, with a total of
153 2,169 stations—approximately six times the number of surface stations available from the NCEP
154 ADP dataset within the Chinese domain. This higher station density significantly enhances the
155 spatial representativeness of near-surface meteorological conditions in the YRD region. Using
156 Observation Nudging assimilation techniques, these datasets collectively correct systemic biases
157 in ERA5's near-surface fields within the WRF framework, enhancing the model's capacity to
158 resolve localized circulation patterns. The AWS data further act as a cross-validation source to
159 quantify YRD1km's accuracy improvements.

160 **2.3 High-resolution Land Cover Geographical Data**

161 Conventional land use datasets in WRF (USGS 1992-1993 or MODIS 2001) (Anderson et
162 al., 1976) are limited in their ability to reflect the rapid urban expansion and evolving land surface

163 characteristics of the YRD region. To address this, we integrate the EWC2020 dataset—a global
164 land cover product with 10-meter spatial resolution that classifies 11 surface types (e.g., built-up
165 areas, croplands, water bodies) (<https://esa-worldcover.org/en>). By updating WRF's land surface
166 parameters with EWC2020, we refine the representation of aerodynamic roughness lengths and
167 urban heat island effects. For instance, reclassifying Shanghai's Pudong district from Moderate
168 Resolution Imaging Spectroradiometer (MODIS) "mixed urban" to EWC2020 "high-intensity
169 built-up" improves wind field simulations by better capturing drag effects from high-rise structures,
170 as validated against AWS observations.

171 **3. Methods**

172 **3.1 WRF Model Configuration for Dynamical Downscaling**

173 This study employs the WRF-ARW model (v4.4.2) (Skamarock et al., 2019) to establish a
174 dynamic downscaling framework, enhancing the spatial resolution of ERA5 reanalysis data from
175 ~31 km to 1 km. The model domain is configured with a triple-nested grid centered at (29.36°N,
176 115.65°E) with horizontal resolutions of 9 km (D01, with 342×305 grid points), 3 km (D02, with
177 529×640 grid points), and 1 km (D03, with 919×949 grid points). The innermost domain, D03,
178 covers the entire YRD region (Figure 1a) and is designed to capture local circulation features
179 associated with urban clusters, lakes, and hilly terrain at a kilometer-scale resolution. Two-way
180 nesting was employed for all three domains to allow feedback between nested grids. All domains
181 were initialized simultaneously, with ERA5 initial conditions interpolated directly onto each
182 domain, including the 1-km grid. In the vertical direction, 61 terrain-following eta levels are used,
183 with the model top set at 10 hPa, which facilitates a detailed resolution of boundary layer dynamics.
184 Based on previous studies (Bernini et al., 2025; Sahu et al., 2025), the following physical
185 parameterization schemes were selected: the Thompson microphysics scheme (Thompson et al.,

186 2008), which is well-suited for high-resolution cloud microphysics; the Dudhia shortwave
187 radiation (Dudhia, 1989) and RRTM longwave radiation schemes (Mlawer et al., 1997) for
188 radiative transfer; and for boundary layer and land surface processes, the YSU non-local closure
189 scheme (Hong et al., 2006) coupled with the Noah land surface model (Tewari et al., 2004), which
190 enhances the representation of near-surface turbulent exchanges. The Kain-Fritsch cumulus
191 parameterization scheme (Kain, 2004) is applied only in the outer grid (D01) to mitigate
192 uncertainties in the “gray zone” below the 3 km grid resolution.

193 To reduce the accumulation of model errors, a cold-start strategy is implemented, with
194 simulations initiated four times daily at 00, 06, 12, and 18 UTC, respectively. Each run generates
195 a continuous 6-hour forecast period, from which the first hour is discarded as model spin-up.
196 Ultimately, this approach produces a continuous hourly three-dimensional wind field dataset.

197 **3.2 Conventional Observational Data Assimilation via Nudging**

198 While WRF dynamical downscaling enhances dataset resolution and preserves dynamical
199 constraints and physical consistency, it struggles to capture fine-scale wind field features over
200 complex underlying surfaces (e.g., urban clusters, water bodies) without dense observational
201 constraints. To address this, this study employs the Four-Dimensional Data Assimilation (FDDA)
202 technique, integrating conventional observations and ERA5 reanalysis fields through a Nudging
203 approach, thereby balancing localized dynamical processes and large-scale circulation consistency.
204 The core formulation of this approach is:

$$205 \quad \frac{\partial x}{\partial t} = F(x) + G \cdot W(t) \cdot (x_{obs} - x) \quad (1)$$

206 where x represents the model variable, $F(x)$ denotes the model dynamical equations, G is the
207 relaxation coefficient, and $W(t)$ is the temporal weighting function.

208 This study adopts a hybrid Nudging scheme combining two strategies: (1) Observation
 209 Nudging (ON): Direct assimilation of in situ observations from CMA AWS and NCEP ADP to
 210 dynamically refine local wind fields. (2) Analysis Nudging (AN): Application of ERA5 reanalysis
 211 fields as constraints to impose large-scale adjustments across the entire model domain hourly
 212 (Stauffer and Seaman, 1990), preventing deviations from large-scale circulation patterns. Thus, the
 213 combined ON+AN assimilation scheme ensures both large-scale consistency and enhanced
 214 regional meteorological representation.

215 Taking the nudging experiment conducted over a continuous four-day period from 1 to 4
 216 June 2022 as an illustrative example, a time window selected to capture representative synoptic
 217 and mesoscale variability, the study quantitatively evaluates wind field accuracy over the YRD
 218 against ground-based observations using three statistical metrics: Mean Absolute Error (MAE),
 219 Root Mean Square Error (RMSE), and the Nash-Sutcliffe Efficiency coefficient (NSE; Nash and
 220 Sutcliffe, 1970), defined as follows:

$$221 \quad MAE = \frac{1}{n} \sum_{i=1}^n |A_i - O_i| \quad (2)$$

$$222 \quad RMSE = \sqrt{\frac{1}{n} \sum_{i=1}^n (A_i - O_i)^2} \quad (3)$$

$$223 \quad NSE = 1 - \frac{\sum_{i=1}^n (A_i - O_i)^2}{\sum_{i=1}^n (O_i - \bar{O})^2} \quad (4)$$

224 where A_i represents simulated values from either ERA5 reanalysis or the dynamically downscaled
 225 results, O_i denotes corresponding in situ observations, n is the total number of spatiotemporally
 226 matched observation–simulation pairs. The NSE metric ranges from $-\infty$ to 1, with values
 227 approaching 1 indicating perfect agreement between simulations and observations. As shown in
 228 Table 1, compared to ERA5 data, the ON+AN assimilated dataset demonstrates significant

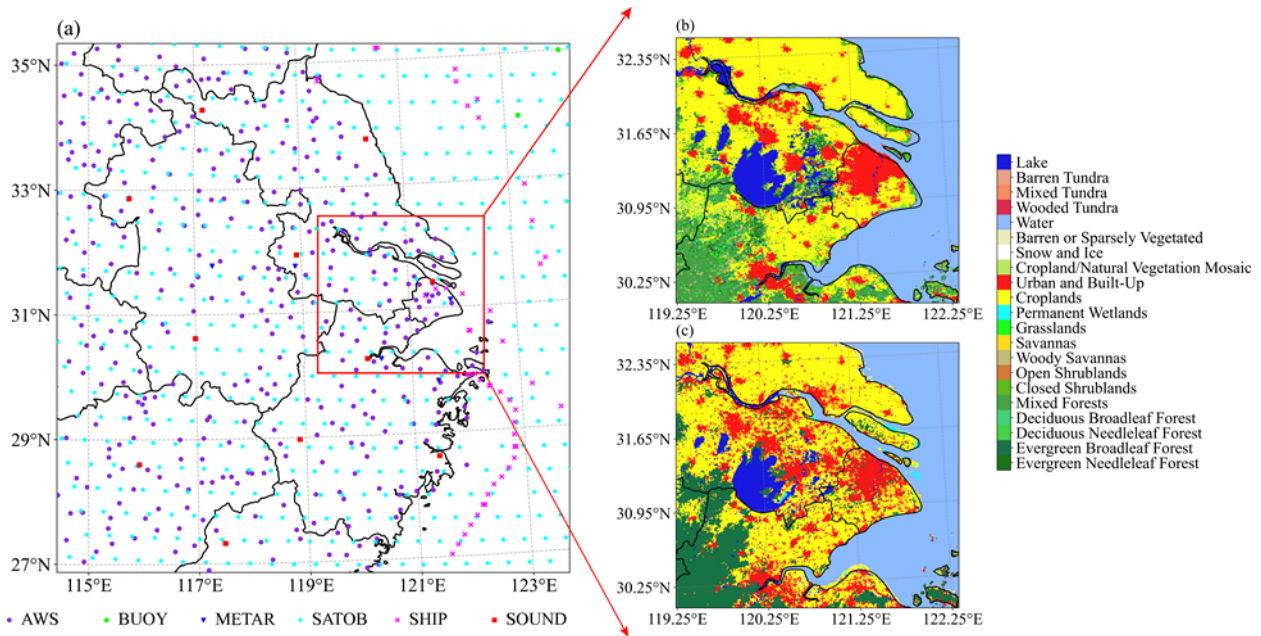
229 improvements across all statistical metrics for both the 10-m zonal (U10m) and meridional (V10m)
 230 wind components. In particular, the MAE is reduced by 22.26% for U10m and 27.45% for V10m,
 231 the RMSE is reduced by 18.38% for U10m and 23.31% for V10m, and the NSE is enhanced by
 232 33.27% for U10m and 41.27% for V10m. These results confirm that the ON+AN hybrid
 233 assimilation scheme substantially enhances the precision of high-resolution wind field datasets in
 234 the YRD region.

235 *Table 1. Comparison of surface (10-m) wind field performance between the ON+AN experiment*
 236 *and ERA5 reanalysis over the YRD region.*

Variable	Sample size	MAE (m/s)		RMSE (m/s)		NSE	
		ERA5	ON+AN	ERA5	ON+AN	ERA5	ON+AN
U10m	33172	1.213	0.943	1.583	1.292	0.504	0.669
V10m	33172	1.388	1.007	1.793	1.375	0.198	0.529

237 **3.3 Impact of High-Resolution Land Use Data Updates**

238 To address the impacts of rapid urbanization on wind field simulations in the YRD, this study
 239 enhances land surface characterization by updating the default MODIS 2001 land use data in the
 240 WRF model with the EWC2020 dataset at 10-meter resolution. Comparative analysis reveals
 241 substantial discrepancies between MODIS 2001 and EWC2020, particularly in Shanghai's
 242 metropolitan core (Figure 1b and 1c). The EWC2020 dataset resolves critical urban morphological
 243 features, including urban sprawl boundaries, park green spaces within city centers, and modified
 244 water-cropland interfaces, thereby more accurately capturing spatial heterogeneity in surface
 245 properties.



246

247 *Figure 1. Spatial distributions of key datasets used in this study. (a) Coverage of the innermost*
 248 *WRF domain (D03, 1-km resolution) over the YRD, along with the distribution of CMA Automatic*
 249 *Weather Stations (AWS) and the spatial coverage of NCEP ADP multi-source conventional*
 250 *observations used for nudging assimilation. The red box shows the region to highlight (b) Land*
 251 *use classification from the default MODIS 2001 dataset in WRF and (c) Updated high-resolution*
 252 *land use classification based on the EWC2020 product.*

253 To quantify land use update effects on wind field simulations, we conduct two experiments
 254 under the ON+AN assimilation framework: 1) LU-MODIS: Retains default MODIS-based land
 255 use types; 2) LU-EWC2020: Incorporates the refined EWC2020-derived surface parameters.
 256 Using the four-day case study, validation metrics (Table 2) demonstrate small but obvious positive
 257 impacts across all metrics for the LU-EWC2020 experiment compared to LU-MODIS. These
 258 results confirm the value of high-resolution land use updates in resolving urbanization-induced
 259 land-atmosphere interactions.

260 *Table 2. Statistical evaluation of land use sensitivity experiments conducted over the YRD region.*

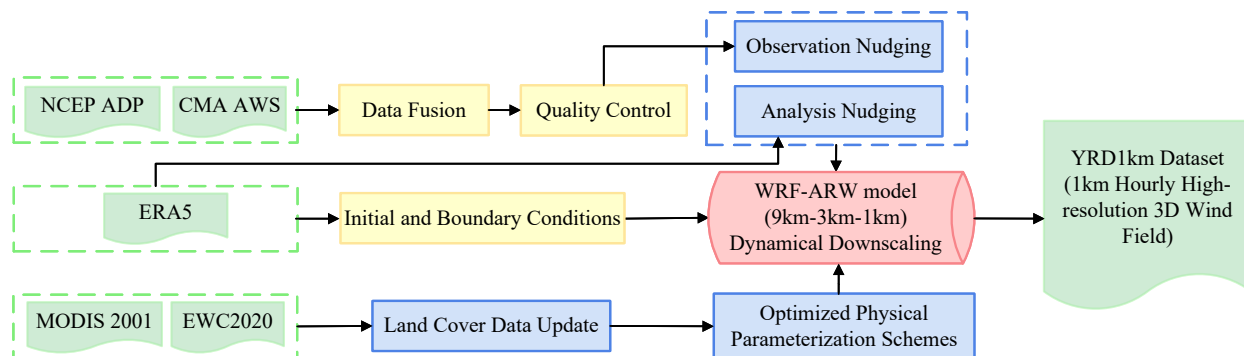
Variable	Sample size	MAE (m/s)		RMSE (m/s)		NSE	
		LU-MODIS	LU-EWC2020	LU-MODIS	LU-EWC2020	LU-MODIS	LU-EWC2020
U10m	33172	0.943	0.935	1.292	1.278	0.669	0.676
V10m	33172	1.007	0.992	1.375	1.355	0.529	0.542

261 **3.4 High-Resolution 3D Wind Field Dataset Generation**

262 Building on the evaluation results in section 3.2 and 3.3, this study develops a systematic
 263 framework for generating the YRD1km dataset over the YRD region, as shown in Figure 2. In the
 264 preprocessing stage, observational constraints for nudging were derived from the integration and
 265 quality control (QC) of NCEP ADP and CMA AWS datasets. Surface parameterization was refined
 266 by replacing the default MODIS 2001 land-use data with the updated EWC 2020 dataset. For
 267 model simulation, ERA5 reanalysis provided the initial and boundary conditions for a triple-nested
 268 WRF configuration (9 km → 3 km → 1 km). The updated surface parameters were used to
 269 optimize the static fields, while a suite of optimized physical schemes and a cold-start initialization
 270 strategy were applied to suppress error accumulation. A hybrid observational nudging scheme (ON
 271 + AN) was employed to enhance the model’s consistency with observed atmospheric states,
 272 resulting in continuous hourly 3D wind vector outputs at 1-km horizontal resolution and 61 vertical
 273 levels during the summer months (June – August) from 2021 to 2023.

274 Comprehensive multi-dimensional validation was performed using both surface station
 275 observations and radiosonde profiles. The near-surface wind simulation performance was assessed
 276 through MAE, RMSE, and NSE metrics, to evaluate the overall, spatial, and temporal accuracy of
 277 the dataset. In addition, radiosonde-derived vertical wind profiles were used to examine the fidelity
 278 of the reconstructed wind field structure in the lower and middle troposphere. Furthermore,
 279 convective case analyses highlight the capability of the YRD1km dataset to capture fine-scale

280 dynamical features, demonstrating clear improvements over ERA5 and underscoring the
 281 effectiveness of the integrated approach in high-resolution wind field reconstruction.



282

283 *Figure 2. The schematic workflow of YRD1km 3D wind field generation.*

284 4. Results and Discussion

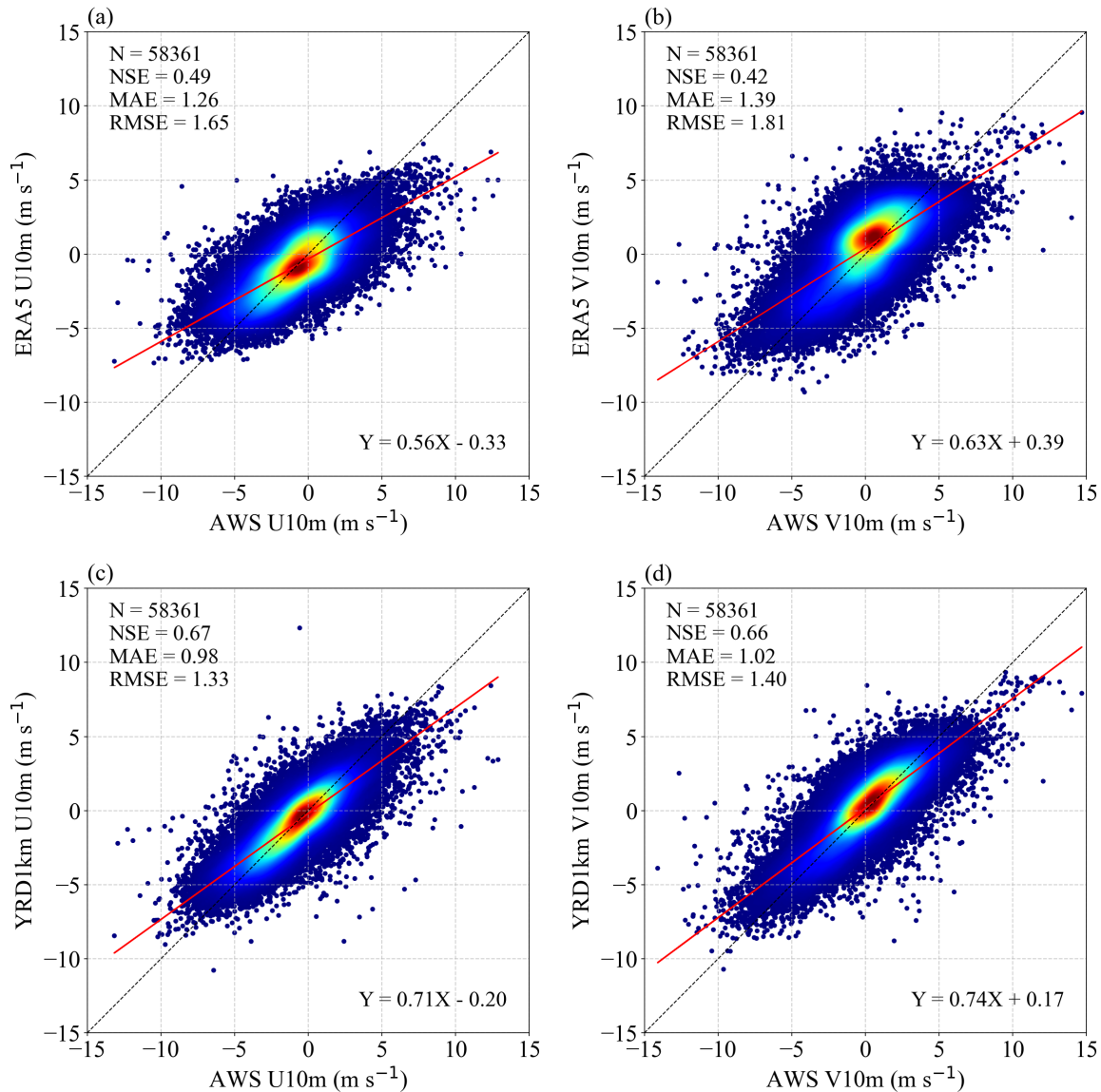
285 4.1 Evaluation of YRD1km High-Resolution Dataset Accuracy

286 4.1.1 Accuracy Evaluation of YRD1km and ERA5 Based on AWS Observations

287 A comprehensive evaluation of near-surface wind field accuracy was conducted using AWS
 288 observations across the YRD region over a one-week period from 1 to 7 June 2022, serving as a
 289 representative example. Due to the different spatial resolutions of YRD1km and ERA5, a nearest-
 290 grid-point matching method was adopted for comparison with station observations (Liu et al.,
 291 2025). As shown in Figure 3, scatterplots of the 10-m wind field U and V components for both
 292 ERA5 and YRD1km datasets were analyzed to assess their respective simulation capabilities.
 293 Overall, YRD1km exhibited superior performance in both U and V components, as evidenced by
 294 higher NSE coefficients, lower MAE and RMSE, and a tighter scatter distribution. Regression
 295 slopes for YRD1km were also notably closer to the 1:1 reference line, indicating a more accurate
 296 representation of the near-surface wind field compared to ERA5. For the U component (Figure 3a,
 297 c), ERA5 presented an NSE of 0.49, with MAE and RMSE of 1.26 m/s and 1.65 m/s, respectively,
 298 and a regression slope of only 0.56, with increasing deviations under higher wind speed conditions.

299 In contrast, YRD1km achieved a significant improvement with an NSE of 0.67, MAE reduced to
300 0.98 m/s, RMSE reduced to 1.33 m/s, and an increased regression slope of 0.71, significantly
301 reducing systematic biases. Further analysis based on the sign of the U component revealed that
302 ERA5 exhibited a consistent underestimation of both easterly winds ($U < 0$) and westerly winds
303 ($U > 0$), particularly under stronger wind conditions ($|U| > 2$ m/s). This finding aligns with previous
304 reports by Hu et al. (2023). While YRD1km also exhibited a similar underestimation pattern, its
305 magnitude was notably reduced, indicating an improved representation of directional wind
306 components compared to ERA5. Additionally, as wind speed increased, scatter dispersion became
307 more pronounced, with fewer samples in the high wind speed range, adding challenges to accurate
308 simulation.

309 For the V component (Figure 3b, d), ERA5 showed an even lower NSE of 0.42, with MAE
310 and RMSE of 1.39 m/s and 1.81 m/s, respectively, and a regression slope of 0.63, indicating a less
311 accurate simulation. Conversely, YRD1km significantly improved the NSE to 0.66, reduced MAE
312 to 1.02 m/s, RMSE to 1.40 m/s, and increased the regression slope to 0.74. Similar to the U
313 component, the V component displayed a directional-dependent error pattern, with an
314 underestimation of both northerly winds ($V < 0$) and southerly winds ($V > 0$), especially under
315 stronger wind conditions. The increasing scatter dispersion and simulation uncertainty with higher
316 wind speeds further highlight the challenges and needs of reproducing complex wind fields.



317

318 *Figure 3. Scatterplot evaluation of 10-m wind components over the YRD region: (a) ERA5*

319

U10m, (b) ERA5 V10m, (c) YRD1km U10m, and (d) YRD1km V10m.

320

Results in Figure 3 are based on hourly data. Considering that climate research emphasizes

321

the use of daily data to smooth short-term fluctuations and reveal long-term trends (Kotlarski et

322

al., 2019; Nashwan et al., 2019; Zhang et al., 2024), this study further examined the simulation

323

accuracy of 10-m wind filed at the daily mean scale. Based on daily mean observations from more

324

than 300 AWS stations across the YRD region over a continuous seven-day period from 1 to 7

325 June 2022 (Table 3), the comparison results demonstrate that YRD1km maintains a consistent
 326 accuracy advantage over ERA5 for all evaluated metrics, including the U and V wind components
 327 as well as 10-m wind speed. Notably, the daily mean values of the U and V components exhibited
 328 better statistical performance than their hourly counterparts, as temporal averaging effectively
 329 mitigates short-term fluctuations and random errors, enhancing simulation stability. Additionally,
 330 compared to 10-m wind speed (WSPD10m), the U and V components demonstrated greater
 331 improvements in error metrics, with NSE values closer to 1. This is primarily because wind speed
 332 is a scalar variable, while U and V components are vectors accounting for wind direction errors.

333 *Table 3. Statistical comparison of daily 10-m wind fields between ERA5 and YRD1km datasets*
 334 *over the YRD region.*

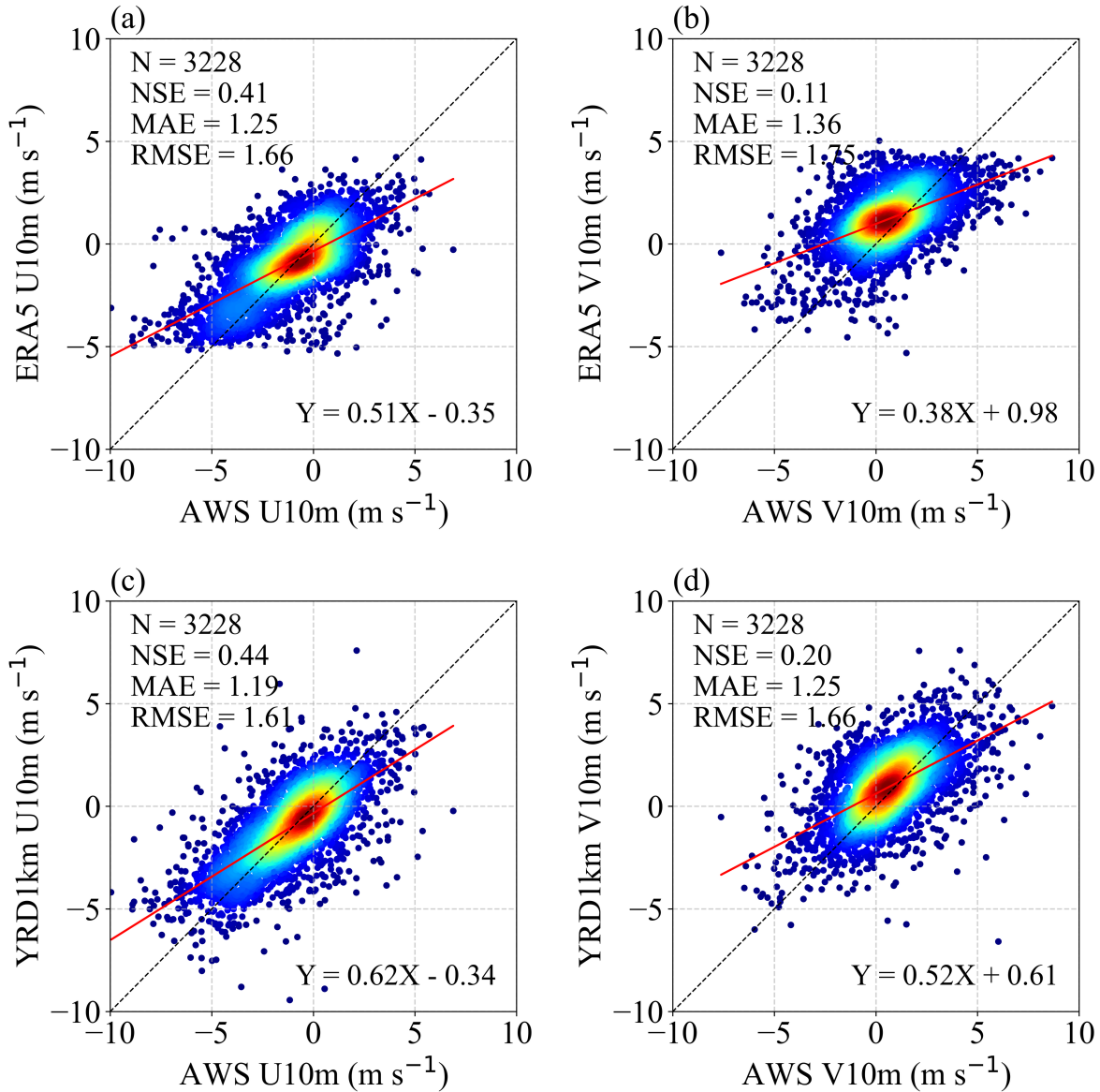
Variable	Indicator	Data		Improvement (%)
		ERA5	YRD1km	
U10m	MAE (m/s)	0.598	0.338	43.48
	RMSE (m/s)	0.783	0.451	42.40
	NSE	0.753	0.918	66.80
V10m	MAE (m/s)	0.716	0.367	48.74
	RMSE (m/s)	0.946	0.498	47.36
	NSE	0.583	0.884	72.18
WSPD10m	MAE (m/s)	0.619	0.422	31.83
	RMSE (m/s)	0.820	0.547	33.29
	NSE	0.470	0.765	55.66

335 4.1.2 Independent Validation

336 To rigorously evaluate the generalization capability of the YRD1km dataset beyond locations
 337 directly constrained by the nudging procedure, we implemented an independent validation strategy
 338 using a subset of AWS stations withheld from the assimilation process. Specifically, approximately

339 10% of the stations employed in the ON+AN nudging experiments were randomly selected and
340 reserved exclusively for independent evaluation, while the remaining stations continued to provide
341 observational constraints for WRF simulations.

342 The independent validation was conducted over a continuous four-day period from 1 to 4
343 June 2022, allowing the evaluation to sample a range of synoptic and mesoscale meteorological
344 conditions. Validation against observations at these withheld stations shows that the YRD1km
345 dataset exhibits improved performance relative to ERA5 in simulating near-surface wind
346 fields. For the U component, NSE increases by 5.08%, MAE decreases by 4.80%, and RMSE
347 decreases by 3.01% relative to ERA5. For the V component, NSE increases by 10.11%, while
348 MAE and RMSE decrease by 8.09% and 5.14%, respectively. In addition, the fitted relationships
349 between simulated and observed U and V components shifted closer to the 1:1 line, indicating
350 enhanced fidelity in reproducing near-surface wind variability (Figure 4). These results indicate
351 that the performance gains in YRD1km are not limited to assimilated locations. Instead, the
352 improvements extend spatially, demonstrating that the combination of dynamical downscaling,
353 high-resolution land-surface updates, and the hybrid ON+AN nudging framework enhances the
354 regional wind field representation in a physically coherent manner.



355

356 *Figure 4. Independent validation scatterplots of 10-m wind components over the YRD region: (a)*

357

ERA5 U10m, (b) ERA5 V10m, (c) YRD1km U10m, and (d) YRD1km V10m.

358 4.1.3 Comparison of spatial variations between YRD1km and ERA5

359

Building upon the preceding quantitative accuracy assessment, the study further examines

360

the spatial variations of near-surface wind fields represented by the YRD1km and ERA5 datasets,

361

as illustrated in Figure 5. Overall, while both datasets (Figure 5a and 5c) adequately capture the

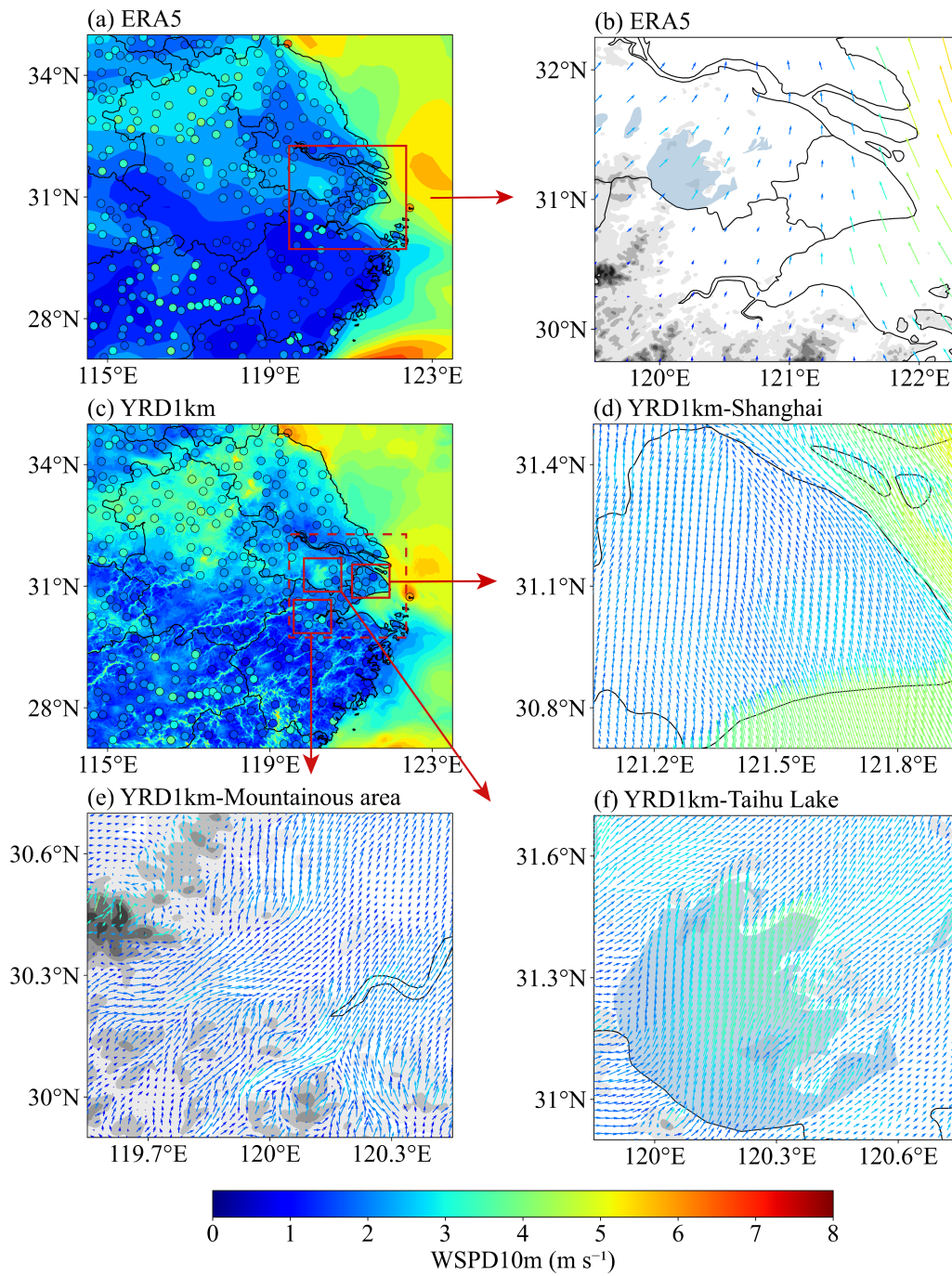
362

large-scale spatial variations of 10-m wind speeds across the YRD, YRD1km demonstrates a

363 notable advantage in resolving mesoscale and local-scale wind field characteristics. Specifically,
364 YRD1km (Figure 5c) offers a much finer spatial representation of wind speed variations compared
365 to ERA5, closely aligned with observational data, particularly over complex terrain and urbanized
366 areas. This includes enhanced wind speed zones over large water bodies such as Lake Taihu,
367 realistic gradients in mountainous regions like southern Anhui and Zhejiang driven by valley flows
368 and orographic effects, as well as improved wind speed structures over highly urbanized areas such
369 as Shanghai. Furthermore, ERA5 exhibits underestimation of wind speed maxima near offshore
370 observation points (e.g., in the East China Sea). YRD1km mitigates these biases through
371 assimilation of AWS data via a nudging approach, enabling better alignment with ground truth
372 observations and significantly enhancing the fidelity of simulated wind fields.

373 These spatial advantages are further highlighted through detailed analyses of wind vector
374 fields. As shown in Figure 5b, ERA5 exhibits an overly smoothed wind field with limited flow
375 differentiation near topographic boundaries. In contrast, the YRD1km dataset presents highly
376 structured and terrain-conforming wind directions. Over the Shanghai metropolitan area (Figure
377 5d), the wind field aligns with urban morphological structures, showing clear directional deflection
378 near city boundaries and dense river network regions, primarily due to thermal forcing and surface
379 drag associated with urbanization. In the mountainous region near Hangzhou (Figure 5e), the wind
380 field captures pronounced curvature and flow separation that closely follow terrain contours,
381 effectively representing multiple terrain-induced processes such as valley and slope winds. Over
382 Lake Taihu (Figure 5f), YRD1km simulates a divergent wind pattern, with significantly higher
383 wind speeds over the lake surface relative to surrounding land, indicative of thermally driven lake–
384 land breeze circulations.

385 Collectively, the spatial patterns observed in both scalar (wind speed) and vector (wind
386 direction) fields strongly affirm the capability of YRD1km to resolve sub-regional atmospheric
387 dynamics. These results further highlight the dataset's potential for supporting a broad spectrum
388 of regional meteorological applications.



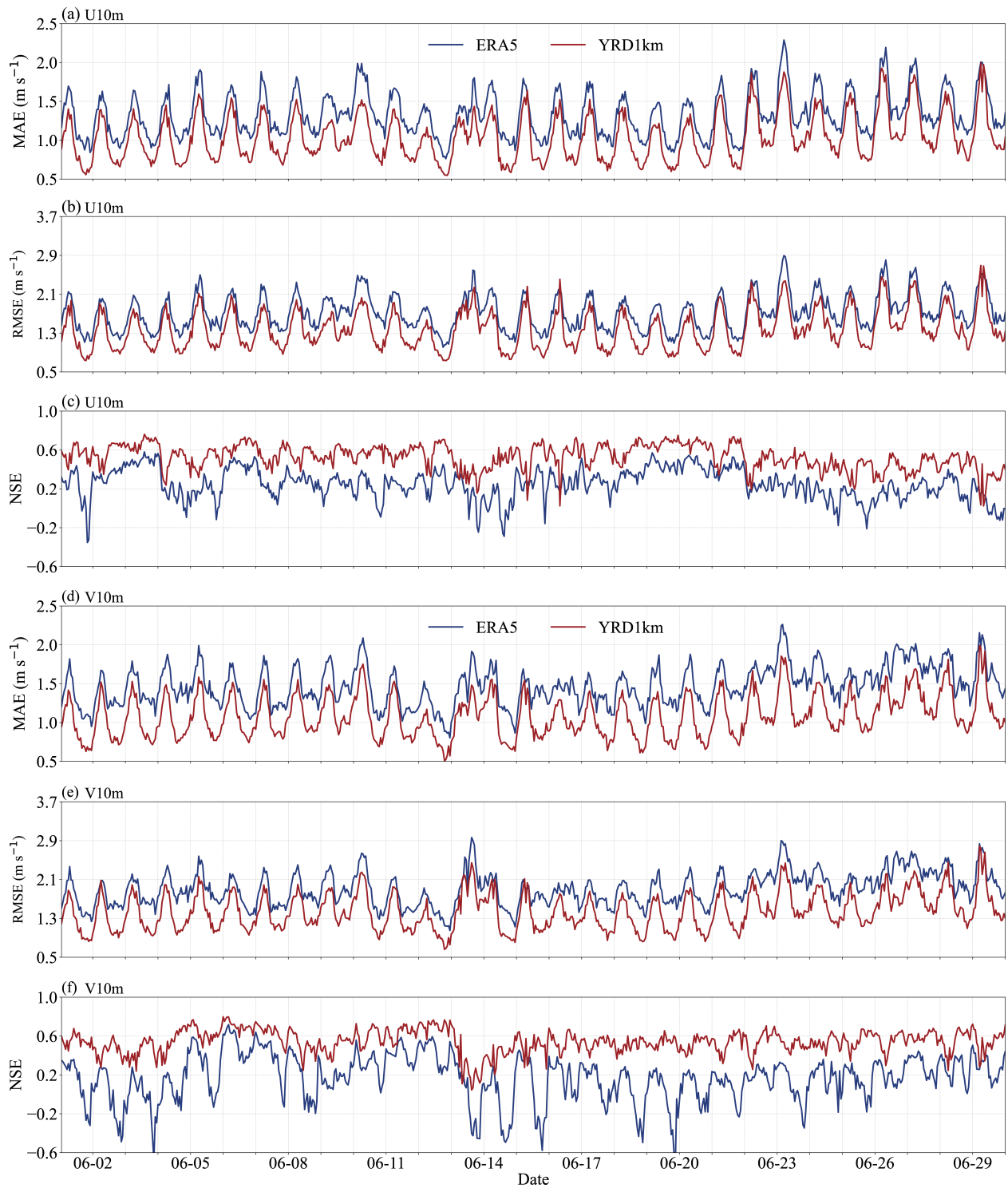
389

390 *Figure 5. Spatial distribution of daily mean near-surface wind fields over the YRD region on 1*
391 *June 2022. Panels (a) and (c) show daily mean 10-m wind speed (WSPD10m) from the ERA5 and*
392 *YRD1km datasets, respectively, overlaid with AWS station observations (colored dots). Panels (b),*
393 *(d), (e), and (f) show locally enlarged wind vector fields: (b) ERA5 over Shanghai and its*
394 *surrounding urban agglomeration; (d) YRD1km over the Shanghai metropolitan area; (e) the*
395 *mountainous region near Hangzhou; and (f) Lake Taihu. Arrows are color-coded by wind speed*
396 *magnitude and overlaid on shaded terrain elevation, with darker tones indicating higher altitudes.*
397 *Major water bodies are shaded in steelblue for clearer identification.*

398 **4.2 Statistical Analysis of the Long-term Time Series of Surface Wind**

399 To assess the temporal performance of the proposed YRD1km dataset, hourly time series
400 analyses of the U10m and V10m wind components were conducted over the YRD region for June
401 2022. For each hour, the performance metrics were computed by spatially averaging errors over
402 all available surface stations within the region. Figures 6 presents the corresponding evolutions of
403 MAE, RMSE and NSE for both wind components, comparing the YRD1km product (red lines)
404 with the ERA5 reanalysis (blue lines), based on validation against ground-based observational data.

405 The YRD1km dataset consistently outperforms ERA5 across both components and all
406 metrics. MAE values for YRD1km remain consistently lower than those of ERA5, particularly
407 during nighttime hours, in agreement with the statistical results summarized in Table 4, which
408 show MAE reductions of 21.61% for U10m and 26.04% for V10m. In addition, the RMSE values
409 for U10m and V10m are reduced by 18.30% and 22.63%, respectively. These results indicate the
410 effectiveness of combining multi-source nudging and high-resolution land use data in consistently
411 capturing subtle wind variations over time.



412

413 *Figure 6. Time series of model performance metrics for hourly 10-m wind components over the*
 414 *YRD region in June 2022. Panels (a), (b) and (c) show the MAE, RMSE and NSE, respectively, for*
 415 *the U10m. Panels (d), (e) and (f) show the corresponding MAE, RMSE and NSE metrics for the*

416 *V10m. All metrics are computed for each hour by spatially averaging errors over all available*
417 *surface stations across the YRD region. The red and blue lines represent the YRD1km and ERA5*
418 *datasets, respectively.*

419 Both wind components exhibit pronounced diurnal cycles in MAE and RMSE, characterized
420 by peak errors during daytime, particularly around local noon, and reduced errors during nighttime.
421 This pattern reflects the influence of boundary layer dynamics, where daytime convective mixing
422 enhances wind variability and poses greater challenges for model accuracy, whereas nocturnal
423 stability leads to more predictable near-surface wind behavior. The persistence and regularity of
424 this fluctuation across the month highlight the necessity of capturing diurnal processes in high-
425 resolution simulations.

426 In terms of NSE, YRD1km maintains higher and more stable values throughout the month
427 for both U10m and V10m. Specifically, NSE values increase by 33.27% for U10m and 40.13% for
428 V10m compared to ERA5. While ERA5 frequently exhibits degraded performance, including
429 negative NSE values during high-variability periods, YRD1km often sustains NSE above 0.4, with
430 frequent peaks exceeding 0.6, especially during nocturnal hours. This reflects a markedly
431 improved temporal agreement between modeled and observed wind variations.

432 Overall, the consistent improvements observed across both horizontal wind components
433 confirm the robustness of the proposed downscaling framework. By effectively addressing both
434 synoptic-scale and diurnal-scale variability, the YRD1km dataset provides a substantially
435 enhanced representation of near-surface wind fields in a complex and highly urbanized region such
436 as the YRD.

437 *Table 4. Evaluation of 10-m wind field simulation performance over the YRD region in June*
438 *2022.*

Variable	Sample size	Indicator	Data		Improvement (%)
			ERA5	YRD1km	
U10m (m/s)	243280	MAE	1.333	1.045	21.61
		RMSE	1.766	1.443	18.30
		NSE	0.468	0.645	33.27
V10m (m/s)	243280	MAE	1.474	1.090	26.04
		RMSE	1.938	1.500	22.63
		NSE	0.407	0.645	40.13

439 4.3 Evaluation of Vertical Wind Profile Accuracy Using Radiosonde Observations

440 To comprehensively evaluate the vertical simulation performance of the YRD1km dataset,
441 radiosonde observations from the Baoshan station in Shanghai (ID: 58362) were used for the
442 month of June 2022 at 00 and 12 UTC. This station is situated at 31.39°N, 121.45°E with an
443 elevation of 3.3 m, within a densely built-up urban area. A comparative analysis was conducted
444 between YRD1km and ERA5 reanalysis data for wind speed accuracy within the 1000–100 hPa
445 pressure range, focusing on both Bias and RMSE metrics. The YRD1km dataset provides outputs
446 at 32 standard vertical levels, ranging from 1000 hPa near the surface to 10 hPa in the upper
447 atmosphere. These levels are obtained through vertical interpolation from the original 61 terrain-
448 following eta levels of the WRF model. Key pressure levels include: 1000, 975, 950, 925, 900,
449 875, 850, 825, 800, 775, 750, 700, 650, 600, 550, 500, 450, 400, 350, 300, 250, 225, 200, 175, 150,
450 125, 100, 70, 50, 30, 20, and 10 hPa.

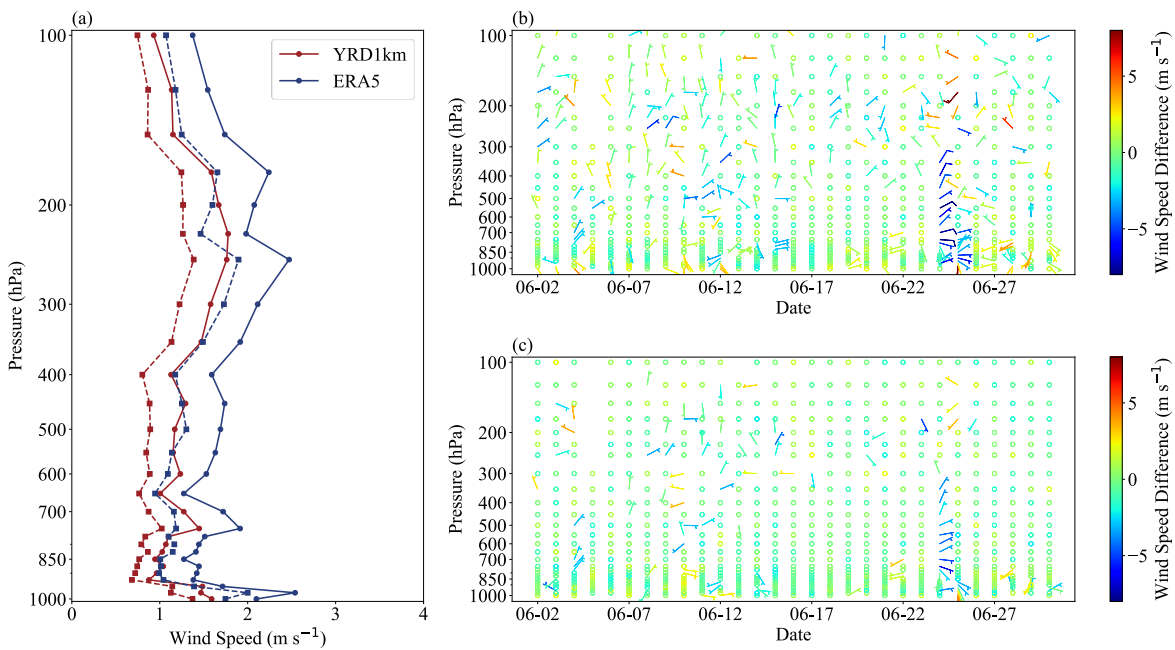
451 As illustrated in Figure 7a, the vertical profiles of MAE (dashed lines) and RMSE (solid
452 lines) reveal that the YRD1km dataset outperforms ERA5 across all pressure levels. The
453 improvements are pronounced in the lower troposphere, benefiting from the dynamic constraints
454 of multi-source observational nudging on near-surface winds and the refined land surface flux

455 representation driven by high-resolution land use data. The maximum reduction in RMSE reaches
456 up to 1.1 m/s at 975 hPa, representing a 42.18% improvement and highlighting the substantial
457 enhancement in near-surface wind speed accuracy provided by YRD1km.

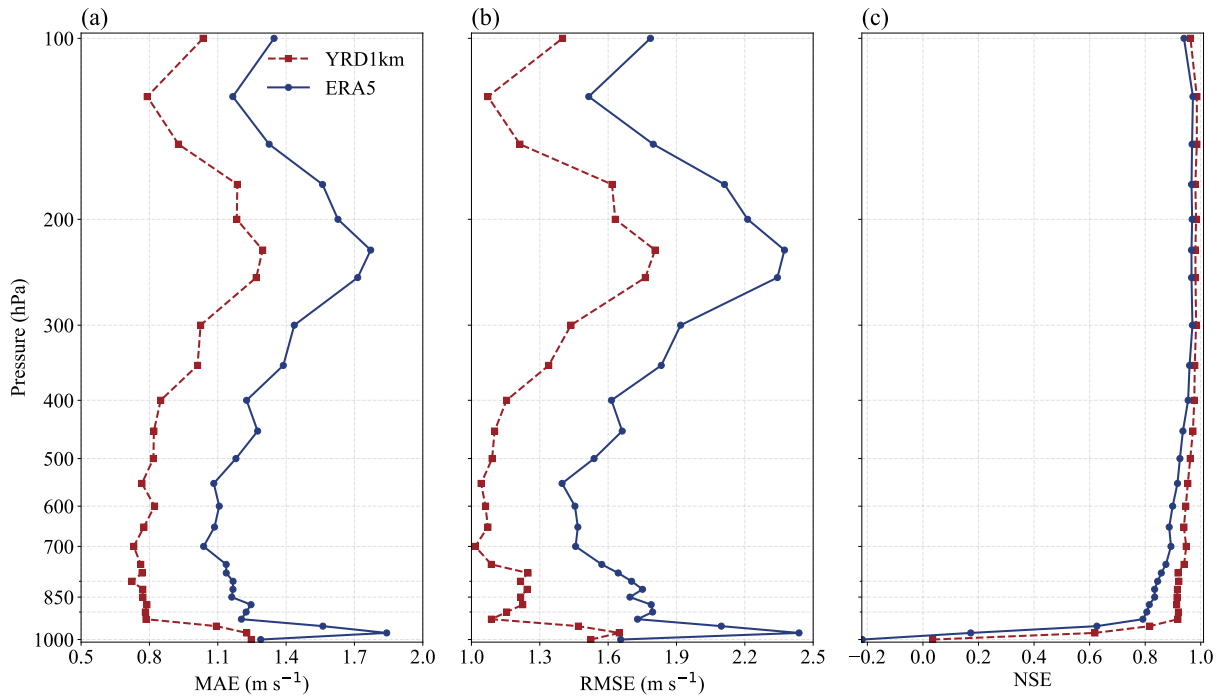
458 Time–height cross-section of wind vector differences plot (Figures 7b and 7c) further
459 highlights the clear performance of YRD1km. In Figure 7b, ERA5 exhibits frequent and large wind
460 speed differences, often exceeding ± 5 m/s, along with abrupt directional shifts, particularly within
461 the near-surface layer. Notably, at 00 UTC on June 24, radiosonde data indicate a sharp wind speed
462 increase above the 950 hPa level, exceeding 19.5 m/s, which ERA5 significantly underestimates.
463 This result is consistent with previous studies that have identified ERA5’s limitations in capturing
464 extreme wind events due to its coarser resolution and less-constrained boundary layer
465 parameterizations (Alkhalidi et al., 2025). In contrast, the YRD1km dataset exhibits a more stable
466 vertical wind structure, with smaller deviations from observed values. Although slight
467 underestimations remain during high wind episodes, the magnitude of extreme discrepancies is
468 considerably reduced compared to ERA5. This improvement underscores the effectiveness of the
469 multi-source observational nudging system in locally constraining vertical wind profiles and
470 enhancing model fidelity.

471 To further assess the representativeness of the vertical performance, we conducted similar
472 validations from all valid sounding samples at 11 radiosonde stations across the Yangtze River
473 Delta are now presented in Figure 8. These statistics show robust and systematic improvements of
474 YRD1km relative to ERA5, including average reductions of approximately 29.64% in MAE, 27.78%
475 in RMSE, and increases of about 47.75% in NSE, confirming that the enhanced 3D wind
476 performance of YRD1km is robust and regionally representative throughout the troposphere.

477 In summary, the YRD1km dataset, developed through the synergistic integration of high-
 478 resolution land surface information and multi-source data assimilation techniques, significantly
 479 improves not only near-surface wind simulations but also the representation of vertical wind
 480 structures. This provides a reliable, high-quality data foundation for a wide range of 3D wind field-
 481 dependent applications, such as low-level wind shear, wind turbine load estimation, pollutant
 482 cross-layer transport modeling, and urban atmospheric environment studies.



483
 484 *Figure 7. Vertical evaluation of wind field performance from the YRD1km and ERA5 datasets*
 485 *against radiosonde observations at the Baoshan station in Shanghai during June 2022. (a) Vertical*
 486 *profiles of wind speed MAE (dashed lines) and RMSE (solid lines) for YRD1km (red) and ERA5*
 487 *(blue), calculated from all available soundings at 00 and 12 UTC. (b) Time–height cross-section*
 488 *of wind vector differences between ERA5 and radiosonde observations (RAOB), with wind speed*
 489 *differences (m/s) indicated by color shading. (c) As in (b), but for YRD1km minus RAOB. Wind*
 490 *difference plots are shown at 24-hour intervals, beginning at 00 UTC on 2 June 2022.*



491

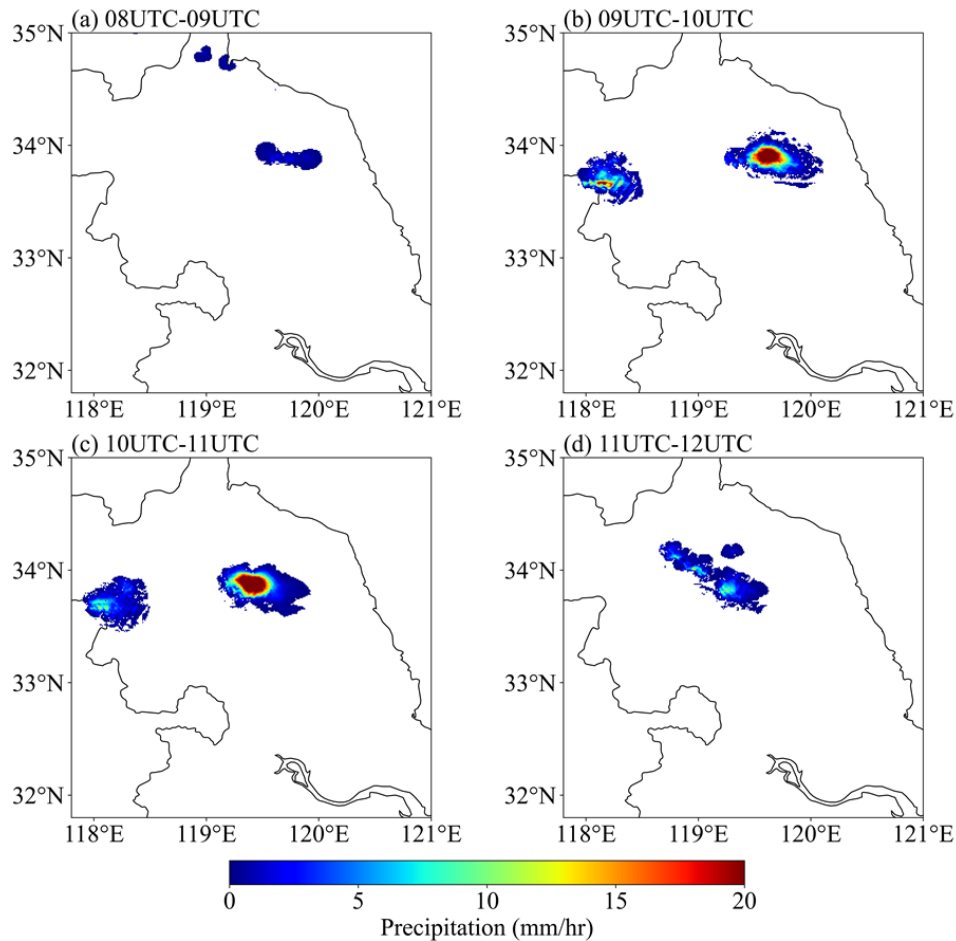
492 **Figure 8.** Vertical evaluation of wind field performance from the YRD1km and ERA5 datasets
 493 against radiosonde observations at 11 stations across the Yangtze River Delta in June 2022. Panels
 494 show (a) MAE, (b) RMSE and (c) NSE, computed using all available 00 UTC and 12 UTC
 495 soundings.

496 4.4 Case Studies of Severe Convection Events

497 While previous statistical validations have demonstrated the superior performance of the
 498 YRD1km dataset spatially and temporally, its advantages are further illustrated in short-term, high-
 499 impact convective events. In such situations, the high spatial and temporal resolution of YRD1km
 500 enables a more detailed diagnosis of mesoscale and vertical dynamical structures associated with
 501 convective initiation and evolution.

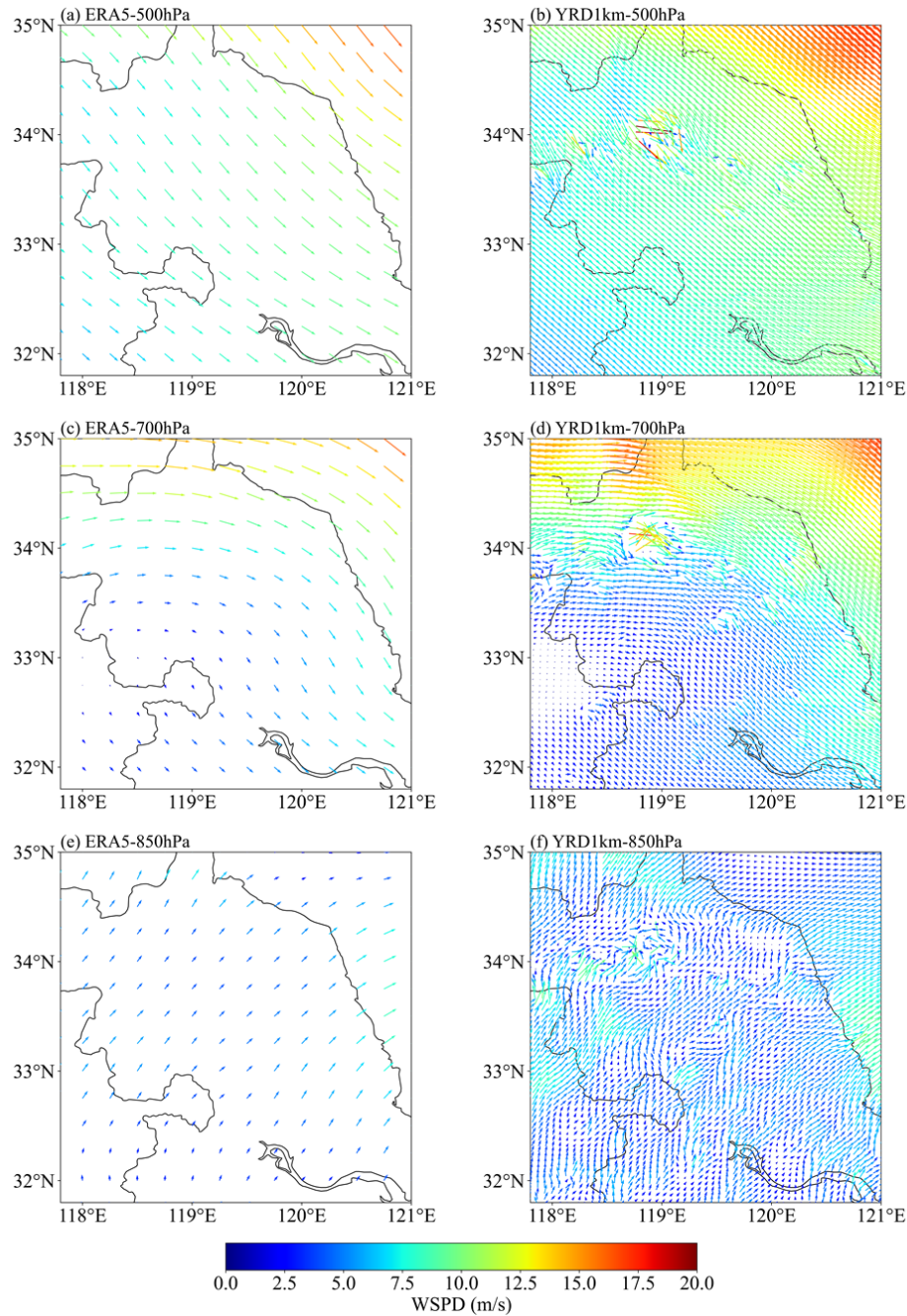
502 As illustrated in Figure 9, based on the China Multi-Source Merged Precipitation Analysis
 503 (CMPAS) dataset, a convective storm outbreak occurred over northern Yancheng, Jiangsu Province,

504 on the afternoon of 16 June 2022. The event was characterized by highly localized and intense
505 precipitation, with peak hourly rainfall rates reaching up to $20 \text{ mm}\cdot\text{h}^{-1}$.



506
507 *Figure 9. Hourly evolution of precipitation associated with a convective storm over northern*
508 *Yancheng, Jiangsu Province, on 16 June 2022.*

509 To investigate the applicability of the YRD1km dataset in high-impact weather scenarios, this
510 study conducts a comparative analysis of wind field structures between ERA5 and YRD1km
511 during the convective event, focusing on three key pressure levels: 500 hPa, 700 hPa, and 850 hPa
512 (Figure 10). These levels are critical for identifying shear lines, low-level jets, and convective
513 initiation mechanisms.



514

515 *Figure 10. Comparative analysis of wind field structures between the YRD1km and ERA5 datasets*

516 *during the short-duration severe convective event over Yancheng, Jiangsu Province. Displayed are*

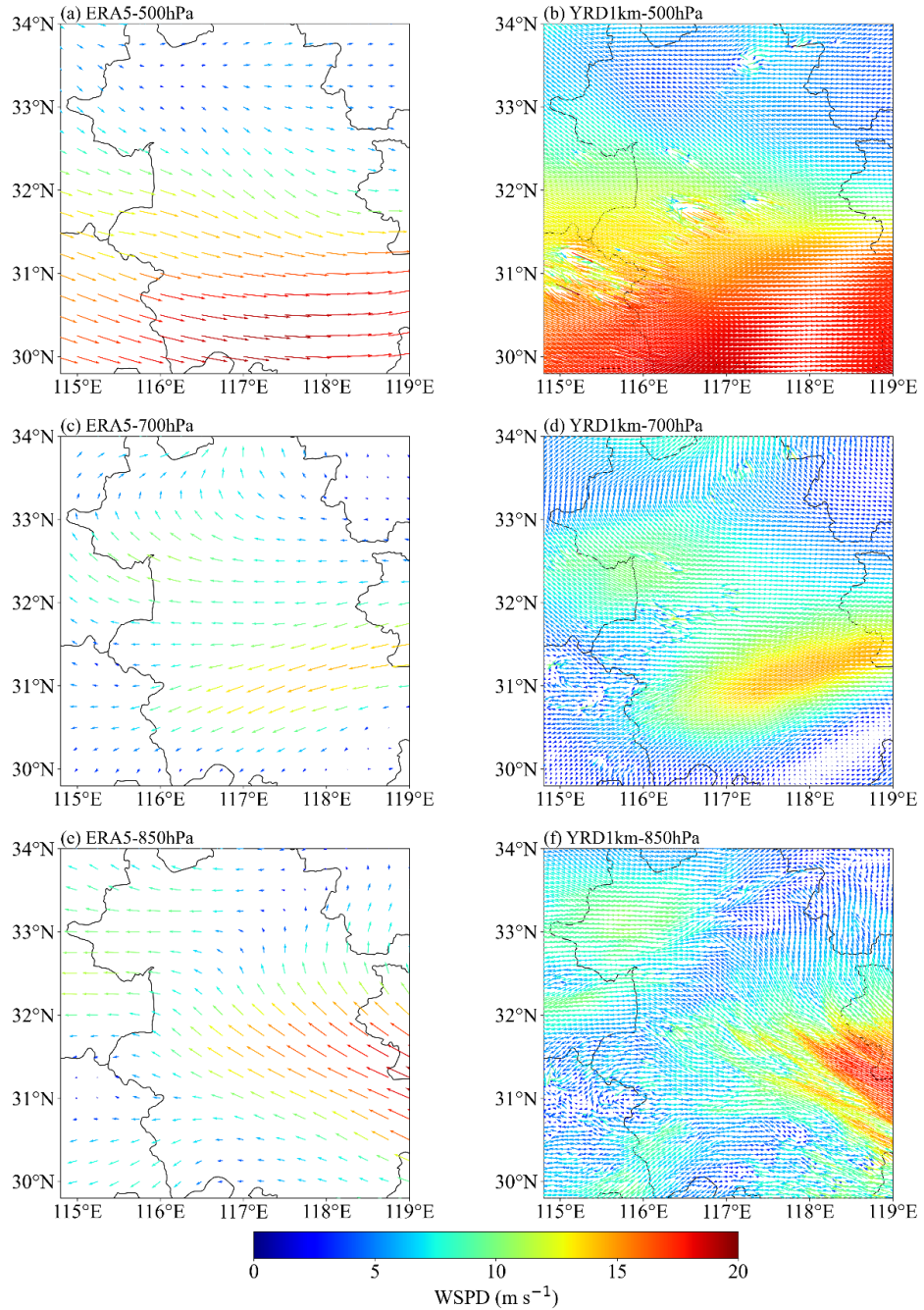
517 *horizontal wind vectors (arrows) and wind speed (color shading) at the (a, b) 500 hPa, (c, d) 700*

518 *hPa, and (e, f) 850 hPa levels from ERA5 (left column) and YRD1km (right column) at 08:00 UTC*

519 *on 16 June 2022. For visual clarity, YRD1km wind vectors have been thinned by a factor of six.*

520 Overall, the wind field structure in ERA5 appears relatively homogeneous, limiting its ability
521 to capture mesoscale and sub-mesoscale disturbances. In contrast, YRD1km reveals more detailed
522 local structures and dynamic features, demonstrating a stronger capacity to resolve mesoscale
523 systems. Across all three pressure levels, YRD1km consistently captures regions of enhanced wind
524 speed, wind shear, and convergence. Notably, near 34°N, 119°E at 500 hPa, YRD1km identifies a
525 localized wind speed maximum exceeding 17.5 m/s and a well-defined shear zone. At 700 hPa, a
526 clear convergence band and wind speed enhancement area are observed, which is conducive to the
527 maintenance and development of the convective system. Although wind speeds weaken at 850 hPa,
528 perturbation signatures remain evident. These structural features spatially align with the center of
529 heavy precipitation during the event, indicating that YRD1km has enhanced diagnostic capability
530 in capturing the dynamical background for the initiation and maintenance of deep convective
531 systems.

532 Similar three-dimensional wind structures and dynamical consistency are also observed in an
533 independent mesoscale convective precipitation event on 10 June 2022 (Figure 11). During the
534 mature stage of this event, YRD1km consistently resolves enhanced wind speed gradients, low-
535 level convergence, and vertically coherent shear structures across the 500, 700, and 850 hPa levels,
536 whereas ERA5 depicts comparatively smooth and spatially homogeneous flow patterns. In
537 particular, YRD1km captures a well-defined low-level jet and its associated convergence zone at
538 850 hPa, together with mesoscale wind speed enhancements at mid-levels. The spatial
539 configuration of these features closely corresponds to the observed organization of convective
540 precipitation, highlighting the ability of YRD1km to represent dynamically relevant structures that
541 are critical for convective system development.



542

543 *Figure 11. Comparative analysis of horizontal wind field structures between ERA5 and YRD1km*

544 *during a mesoscale convective precipitation event over the study region on 10 June 2022. Shown*

545 *are horizontal wind vectors (arrows) and wind speed (color shading) at the (a, b) 500 hPa, (c, d)*

546 *700 hPa, and (e, f) 850 hPa levels from ERA5 (left column) and YRD1km (right column) at 04:00*

547 *UTC, corresponding to the mature stage of the convective system. For visual clarity, wind vectors*
548 *in YRD1km are thinned by a factor of six.*

549 Collectively, these case analyses demonstrate that the high spatial resolution of YRD1km
550 enables a physically consistent depiction of three-dimensional wind field structures during severe
551 convective events. Such capability supports its use in diagnostic studies of mesoscale and
552 convective-scale dynamics, and provides a valuable background wind field for applications
553 including high-resolution air-quality dispersion modeling, event-based wind hazard assessment,
554 and the development of training datasets for data-driven downscaling approaches.

555 **5. Conclusions**

556 This study developed and rigorously validated YRD1km, a high-resolution (1 km, hourly)
557 3D wind field dataset over the YRD region. The dataset was generated through dynamical
558 downscaling of ERA5 reanalysis data using a customized WRF model configuration. It was further
559 refined by integrating multi-source observational nudging and updated land use representations to
560 improve surface parameterization.

561 Comprehensive validations using surface station and radiosonde observations confirmed that
562 YRD1km significantly outperforms ERA5 in both near-surface and vertical wind simulations. For
563 10-m wind fields, YRD1km consistently achieved smaller errors and higher skill scores across
564 MAE, RMSE, and NSE, at both hourly and daily scales. The dataset also better characterizes
565 spatial variability in wind speed, particularly over complex terrain and densely urbanized areas.
566 Its wind vector fields align well with underlying geographic features, and monthly statistics show
567 reductions in MAE and RMSE of approximately 20%, with NSE improved by more than 33%. In
568 the vertical dimension, YRD1km exhibited reduced RMSE across nearly all pressure levels and
569 produced observation-consistent vertical profiles. Analyses of severe convective events

570 demonstrated YRD1km’s ability to resolve fine-scale dynamic signatures, including wind shear,
571 low-level convergence, and enhanced wind zones, supporting improved diagnosis of convective
572 development mechanisms.

573 These findings highlight the value of high-resolution wind datasets that integrate physically
574 consistent dynamical downscaling with observational constraints in representing mesoscale and
575 diurnal wind variability over complex urbanized environments. The YRD1km dataset provides a
576 robust, physically coherent foundation for applications that require detailed three-dimensional
577 wind information, including wind energy resource assessment, urban boundary-layer diagnostics,
578 and high-resolution air quality and pollutant dispersion modeling. In particular, the resolved fine-
579 scale vertical wind structures offer important potential for diagnosing low-level wind shear and
580 related dynamical features, which are critical for understanding urban atmospheric processes and
581 for supporting safety-oriented analyses relevant to low-altitude airspace operations in rapidly
582 developing metropolitan regions.

583 Looking ahead, the proposed framework can be further extended to generate longer-term,
584 seasonally continuous high-resolution wind datasets and applied to other regions with complex
585 terrain and heterogeneous land use. Future developments may also incorporate additional
586 observational constraints, such as satellite-based wind products and higher-frequency ground-
587 based remote sensing measurements. In addition, the YRD1km dataset can serve as a physically
588 consistent reference or training dataset for emerging data-driven downscaling approaches,
589 including machine learning models and sub-kilometer-scale simulations, thereby supporting next-
590 generation high-resolution atmospheric modeling and applied research.

591

592 **Data availability**

593 The YRD1km 3D wind field dataset is available at <https://doi.org/10.57760/sciencedb.23752>

594 (Zhang et al., 2025).

595

596 **Author contributions**

597 ZZ: data collection and processing; methodology and analysis; writing (original draft preparation).

598 YL: conceptualization; supervision; methodology and analysis; writing (original draft preparation,

599 review, and editing). XM, PX, and JZ: data collection. ZL, MM, DD, and BL: writing (review and

600 editing). JL: supervision; writing (review and editing).

601

602 **Competing interests**

603 The contact author has declared that none of the authors has any competing interests.

604

605 **Acknowledgments**

606 We gratefully acknowledge the ECNU Multifunctional Platform for Innovation 001 for providing

607 high-performance computing resources. We also thank the ECMWF for access to the ERA5

608 reanalysis data, the NCEP for the global upper air and surface weather observations, the CMA for

609 providing AWS data, and the ESA for the WorldCover 2020 land use data. Finally, we sincerely

610 thank the editor and anonymous reviewers for their insightful comments and constructive

611 suggestions, which greatly improved the quality of this manuscript.

612

613 **Financial support**

614 This research was supported by the National Natural Science Foundation of China (Grant Nos.
615 U2542201 and 42575164) and the Shanghai Science and Technology Program (Grant No.
616 25ZR1401099).

617

618 **References**

619 Alkhalidi, M., Al-Dabbous, A., Al-Dabbous, S., and Alzaid, D.: Evaluating the Accuracy of the
620 ERA5 Model in Predicting Wind Speeds Across Coastal and Offshore Regions, *J. Mar. Sci. Eng.*,
621 13, 149, <https://doi.org/10.3390/jmse13010149>, 2025.

622 Anderson, J. T., Hardy, E. E., Roach, J. T., and Witmer, R. E.: A land use and land cover
623 classification system for use with remote sensor data, Professional Paper, U.S. Geological Survey,
624 <https://doi.org/10.3133/pp964>, 1976.

625 Bao, J., Feng, J., and Wang, Y.: Dynamical downscaling simulation and future projection of
626 precipitation over China, *J. Geophys. Res. Atmospheres*, 120, 8227–8243,
627 <https://doi.org/10.1002/2015JD023275>, 2015.

628 Bernini, L., Lagasio, M., Milelli, M., Oberto, E., Parodi, A., Hachinger, S., Kranzlmüller, D., and
629 Tartaglione, N.: Convection-permitting dynamical downscaling of ERA5 for Europe and the
630 Mediterranean basin, *Quarterly Journal of the Royal Meteorological Society*, 151, e5014,
631 <https://doi.org/10.1002/qj.5014>, 2025.

632 Boé, J., Terray, L., Habets, F., and Martin, E.: Statistical and dynamical downscaling of the Seine
633 basin climate for hydro-meteorological studies, *Int. J. Climatol.*, 27, 1643–1655,
634 <https://doi.org/10.1002/joc.1602>, 2007.

635 Collier, E. and Mölg, T.: BAYWRF: a high-resolution present-day climatological atmospheric
636 dataset for Bavaria, *Earth Syst. Sci. Data*, 12, 3097–3112, [https://doi.org/10.5194/essd-12-3097-](https://doi.org/10.5194/essd-12-3097-2020)
637 2020, 2020.

638 Daescu, D. N. and Langland, R. H.: Error covariance sensitivity and impact estimation with adjoint
639 4D-Var: theoretical aspects and first applications to NAVDAS-AR, *Q. J. R. Meteorol. Soc.*, 139,
640 226–241, <https://doi.org/10.1002/qj.1943>, 2013.

641 Dayon, G., Boé, J., and Martin, E.: Transferability in the future climate of a statistical downscaling
642 method for precipitation in France, *J. Geophys. Res. Atmospheres*, 120, 1023–1043,
643 <https://doi.org/10.1002/2014JD022236>, 2015.

644 De Bode, M., Hedde, T., Roubin, P., and Durand, P.: A Method to Improve Land Use
645 Representation for Weather Simulations Based on High-Resolution Data Sets—Application to

646 Corine Land Cover Data in the WRF Model, *Earth Space Sci.*, 10, e2021EA002123,
647 <https://doi.org/10.1029/2021EA002123>, 2023.

648 Dudhia, J.: Numerical Study of Convection Observed during the Winter Monsoon Experiment
649 Using a Mesoscale Two-Dimensional Model, *J. Atmospheric Sci.*, 46, 3077–3107,
650 [https://doi.org/10.1175/1520-0469\(1989\)046<3077:NSOCOD>2.0.CO;2](https://doi.org/10.1175/1520-0469(1989)046<3077:NSOCOD>2.0.CO;2), 1989.

651 Dujardin, J. and Lehning, M.: Wind-Topo: Downscaling near-surface wind fields to high-
652 resolution topography in highly complex terrain with deep learning, *Q. J. R. Meteorol. Soc.*, 148,
653 1368–1388, <https://doi.org/10.1002/qj.4265>, 2022.

654 Dupuy, F., Durand, P., and Hedde, T.: Downscaling of surface wind forecasts using convolutional
655 neural networks, *Nonlinear Process. Geophys.*, 30, 553–570, [https://doi.org/10.5194/npg-30-553-](https://doi.org/10.5194/npg-30-553-2023)
656 2023, 2023.

657 Fu, D., Liu, Y., Li, H., Liu, S., Li, B., Thapa, S., Yabo, S., Sun, X., Tang, B., Zuo, J., Qi, H., and
658 Tian, C.: Evaluating the Impacts of Land Cover and Soil Texture Changes on Simulated Surface
659 Wind and Temperature, *Earth Space Sci.*, 7, e2020EA001173,
660 <https://doi.org/10.1029/2020EA001173>, 2020.

661 Golzio, A., Ferrarese, S., Cassardo, C., Diolaiuti, G. A., and Pelfini, M.: Land-Use Improvements
662 in the Weather Research and Forecasting Model over Complex Mountainous Terrain and
663 Comparison of Different Grid Sizes, *Bound.-Layer Meteorol.*, 180, 319–351,
664 <https://doi.org/10.1007/s10546-021-00617-1>, 2021.

665 Gutowski, W. J., Ullrich, P. A., Hall, A., Leung, L. R., O'Brien, T. A., Patricola, C. M., Arritt, R.
666 W., Bukovsky, M. S., Calvin, K. V., Feng, Z., Jones, A. D., Kooperman, G. J., Monier, E., Pritchard,
667 M. S., Pryor, S. C., Qian, Y., Rhoades, A. M., Roberts, A. F., Sakaguchi, K., Urban, N., and
668 Zarzycki, C.: The Ongoing Need for High-Resolution Regional Climate Models: Process
669 Understanding and Stakeholder Information, *Bull. Am. Meteorol. Soc.*, 101, E664–E683,
670 <https://doi.org/10.1175/bams-d-19-0113.1>, 2020.

671 Harkey, M. and Holloway, T.: Constrained dynamical downscaling for assessment of climate
672 impacts, *J. Geophys. Res. Atmospheres*, 118, 2136–2148, <https://doi.org/10.1002/jgrd.50223>,
673 2013.

674 Hersbach, H., Bell, B., Berrisford, P., Hirahara, S., Horányi, A., Muñoz-Sabater, J., Nicolas, J.,
675 Peubey, C., Radu, R., Schepers, D., Simmons, A., Soci, C., Abdalla, S., Abellan, X., Balsamo, G.,
676 Bechtold, P., Biavati, G., Bidlot, J., Bonavita, M., De Chiara, G., Dahlgren, P., Dee, D.,
677 Diamantakis, M., Dragani, R., Flemming, J., Forbes, R., Fuentes, M., Geer, A., Haimberger, L.,
678 Healy, S., Hogan, R. J., Hólm, E., Janisková, M., Keeley, S., Laloyaux, P., Lopez, P., Lupu, C.,
679 Radnoti, G., de Rosnay, P., Rozum, I., Vamborg, F., Villaume, S., and Thépaut, J.-N.: The ERA5
680 global reanalysis, *Q. J. R. Meteorol. Soc.*, 146, 1999–2049, <https://doi.org/10.1002/qj.3803>, 2020.

681 Höhle, K., Kern, M., Hewson, T., and Westermann, R.: A comparative study of convolutional
682 neural network models for wind field downscaling, *Meteorol. Appl.*, 27, e1961,
683 <https://doi.org/10.1002/met.1961>, 2020.

684 Hoke, J. E. and Anthes, R. A.: The Initialization of Numerical Models by a Dynamic-Initialization
685 Technique, *Mon. Weather Rev.*, 104, 1551–1556, [https://doi.org/10.1175/1520-](https://doi.org/10.1175/1520-0493(1976)104<1551:tionmb>2.0.co;2)
686 0493(1976)104<1551:tionmb>2.0.co;2, 1976.

687 Hong, S.-Y., Noh, Y., and Dudhia, J.: A New Vertical Diffusion Package with an Explicit Treatment
688 of Entrainment Processes, *Mon. Weather Rev.*, 134, 2318–2341,
689 <https://doi.org/10.1175/mwr3199.1>, 2006.

690 Horvath, K., Koracin, D., Vellore, R., Jiang, J., and Belu, R.: Sub-kilometer dynamical
691 downscaling of near-surface winds in complex terrain using WRF and MM5 mesoscale models, *J.*
692 *Geophys. Res. Atmospheres*, 117, <https://doi.org/10.1029/2012JD017432>, 2012.

693 Hu, W., Scholz, Y., Yeligeti, M., Bremen, L. von, and Deng, Y.: Downscaling ERA5 wind speed
694 data: a machine learning approach considering topographic influences, *Environ. Res. Lett.*, 18,
695 094007, <https://doi.org/10.1088/1748-9326/aceb0a>, 2023.

696 Jung, C. and Schindler, D.: On the influence of wind speed model resolution on the global technical
697 wind energy potential, *Renew. Sustain. Energy Rev.*, 156, 112001,
698 <https://doi.org/10.1016/j.rser.2021.112001>, 2022.

699 Kain, J. S.: The Kain–Fritsch Convective Parameterization: An Update, *J. Appl. Meteorol.*, 43,
700 170–181, [https://doi.org/10.1175/1520-0450\(2004\)043<0170:TKCPAU>2.0.CO;2](https://doi.org/10.1175/1520-0450(2004)043<0170:TKCPAU>2.0.CO;2), 2004.

701 Kotlarski, S., Szabó, P., Herrera, S., Rätty, O., Keuler, K., Soares, P. M., Cardoso, R. M., Bosshard,
702 T., Pagé, C., Boberg, F., Gutiérrez, J. M., Isotta, F. A., Jaczewski, A., Kreienkamp, F., Liniger, M.
703 A., Lussana, C., and Pianko-Kluczyńska, K.: Observational uncertainty and regional climate
704 model evaluation: A pan-European perspective, *Int. J. Climatol.*, 39, 3730–3749,
705 <https://doi.org/10.1002/joc.5249>, 2019.

706 Lei, L. and Hacker, J. P.: Nudging, Ensemble, and Nudging Ensembles for Data Assimilation in
707 the Presence of Model Error, *Mon. Weather Rev.*, 143, 2600–2610, [https://doi.org/10.1175/MWR-](https://doi.org/10.1175/MWR-D-14-00295.1)
708 D-14-00295.1, 2015.

709 Lian, J., Huang, S., Shao, J., Chen, P., Tang, S., Lu, Y., and Yu, H.: TerraWind: A Deep Learning-
710 Based Near-Surface Winds Downscaling Model for Complex Terrain Region, *Geophys. Res. Lett.*,
711 51, e2024GL112124, <https://doi.org/10.1029/2024GL112124>, 2024.

712 Liu, J., Shi, C., Ge, L., Tie, R., Chen, X., Zhou, T., Gu, X., and Shen, Z.: Enhanced Wind Field
713 Spatial Downscaling Method Using UNET Architecture and Dual Cross-Attention Mechanism,
714 *Remote Sens.*, 16, 1867, <https://doi.org/10.3390/rs16111867>, 2024a.

715 Liu, S., Zeman, C., and Schär, C.: Dynamical Downscaling of Climate Simulations in the Tropics,
716 *Geophys. Res. Lett.*, 51, e2023GL105733, <https://doi.org/10.1029/2023GL105733>, 2024b.

717 Liu, Y., Di, D., Li, J., Li, Z., Ma, Z., Zheng, J., Liu, Y.-A., and Zhang, T.: Consistency Assessment
718 of the Winds in Reanalysis Datasets and the GIIRS Product Using Radiosondes, *Adv. Atmospheric*
719 *Sci.*, <https://doi.org/10.1007/s00376-025-4138-x>, 2025.

720 Lo, J. C., Yang, Z., and Pielke, R. A.: Assessment of three dynamical climate downscaling methods
721 using the Weather Research and Forecasting (WRF) model, *J. Geophys. Res. Atmospheres*, 113,
722 2007JD009216, <https://doi.org/10.1029/2007JD009216>, 2008.

723 Mlawer, E. J., Taubman, S. J., Brown, P. D., Iacono, M. J., and Clough, S. A.: Radiative transfer
724 for inhomogeneous atmospheres: RRTM, a validated correlated-k model for the longwave, *J.*
725 *Geophys. Res. Atmospheres*, 102, 16663–16682, <https://doi.org/10.1029/97JD00237>, 1997.

726 Molina, M. O., Gutiérrez, C., and Sánchez, E.: Comparison of ERA5 surface wind speed
727 climatologies over Europe with observations from the HadISD dataset, *Int. J. Climatol.*, 41, 4864–
728 4878, <https://doi.org/10.1002/joc.7103>, 2021.

729 Nash, J. E. and Sutcliffe, J. V.: River flow forecasting through conceptual models part I — A
730 discussion of principles, *J. Hydrol.*, 10, 282–290, [https://doi.org/10.1016/0022-1694\(70\)90255-6](https://doi.org/10.1016/0022-1694(70)90255-6),
731 1970.

732 Nashwan, M. S., Shahid, S., and Chung, E.-S.: Development of high-resolution daily gridded
733 temperature datasets for the central north region of Egypt, *Sci. Data*, 6, 138,
734 <https://doi.org/10.1038/s41597-019-0144-0>, 2019.

735 Sahu, R. K., Bangalath, H. K., Mostamandi, S., Evans, J., Kucera, P. A., and Beck, H. E.:
736 Evaluating microphysics and boundary layer schemes in WRF: assessment of 36 scheme
737 combinations for 17 major storms in Saudi Arabia, *EGUsphere* [preprint],
738 <https://doi.org/10.5194/egusphere-2025-912>, 2025.

739 Santos-Alamillos, F. J., Pozo-Vázquez, D., Ruiz-Arias, J. A., and Tovar-Pescador, J.: Influence of
740 land-use misrepresentation on the accuracy of WRF wind estimates: Evaluation of GLCC and
741 CORINE land-use maps in southern Spain, *Atmospheric Res.*, 157, 17–28,
742 <https://doi.org/10.1016/j.atmosres.2015.01.006>, 2015.

743 Siewert, J. and Kroszczynski, K.: Evaluation of High-Resolution Land Cover Geographical Data
744 for the WRF Model Simulations, *Remote Sens.*, 15, 2389, <https://doi.org/10.3390/rs15092389>,
745 2023.

746 Skamarock, W. C., Klemp, J. B., Dudhia, J., Gill, D. O., Liu, Z., Berner, J., Wang, W., Powers, J.
747 G., Duda, M. G., Barker, D. M., and Huang, X.-Y.: A Description of the Advanced Research WRF
748 Model Version 4, <https://doi.org/10.5065/1DFH-6P97>, 2019.

749 Sun, Y., Deng, K., Ren, K., Liu, J., Deng, C., and Jin, Y.: Deep learning in statistical downscaling
750 for deriving high spatial resolution gridded meteorological data: A systematic review, *ISPRS J.*
751 *Photogramm. Remote Sens.*, 208, 14–38, <https://doi.org/10.1016/j.isprsjprs.2023.12.011>, 2024.

752 Tang, J., Niu, X., Wang, S., Gao, H., Wang, X., and Wu, J.: Statistical downscaling and dynamical
753 downscaling of regional climate in China: Present climate evaluations and future climate
754 projections, *J. Geophys. Res. Atmospheres*, 121, 2110–2129,
755 <https://doi.org/10.1002/2015JD023977>, 2016.

756 Tareghian, R. and Rasmussen, P. F.: Statistical downscaling of precipitation using quantile
757 regression, *J. Hydrol.*, 487, 122–135, <https://doi.org/10.1016/j.jhydrol.2013.02.029>, 2013.

758 Tewari A. M., Chen A. F., Wang A. W., Dudhia A. J., LeMone A. M. A., Mitchell A. K. E., Ek A.
759 M. B., Gayno A. G., Wegiel A. J. W., Cuenca A. R., and Society S. A. M.: Implementation and
760 verification of the unified Noah land-surface model in the WRF model, 20th Conference on
761 Weather Analysis and Forecasting/16th Conference on Numerical Weather Prediction, Seattle, WA:
762 American Meteorological Society, 2004.

763 Thompson, G., Field, P. R., Rasmussen, R. M., and Hall, W. D.: Explicit Forecasts of Winter
764 Precipitation Using an Improved Bulk Microphysics Scheme. Part II: Implementation of a New
765 Snow Parameterization, *Mon. Weather Rev.*, 136, 5095–5115,
766 <https://doi.org/10.1175/2008mwr2387.1>, 2008.

767 Viterbo, F., Sperati, S., Vitali, B., D’Amico, F., Cavalleri, F., Bonanno, R., and Lacavalla, M.:
768 MERIDA HRES: A new high-resolution reanalysis dataset for Italy, *Meteorol. Appl.*, 31, e70011,
769 <https://doi.org/10.1002/met.70011>, 2024.

770 Xu, Z., Han, Y., Tam, C.-Y., Yang, Z.-L., and Fu, C.: Bias-corrected CMIP6 global dataset for
771 dynamical downscaling of the historical and future climate (1979–2100), *Sci. Data*, 8, 293,
772 <https://doi.org/10.1038/s41597-021-01079-3>, 2021.

773 Yuan, H., Cheng, L., Pan, Y., Tan, Z., Liu, Q., and Jin, Z.: A multi-level parallel approach to
774 increase the computation efficiency of a global ocean temperature dataset reconstruction, *J.*
775 *Parallel Distrib. Comput.*, 192, 104938, <https://doi.org/10.1016/j.jpdc.2024.104938>, 2024.

776 Zamo, M., Bel, L., Mestre, O., and Stein, J.: Improved Gridded Wind Speed Forecasts by Statistical
777 Postprocessing of Numerical Models with Block Regression, *Weather Forecast.*, 31, 1929–1945,
778 <https://doi.org/10.1175/waf-d-16-0052.1>, 2016.

779 Zhang, J., Liu, B., Ren, S., Han, W., Ding, Y., and Peng, S.: A 4 km daily gridded meteorological
780 dataset for China from 2000 to 2020, *Sci. Data*, 11, 1230, [https://doi.org/10.1038/s41597-024-](https://doi.org/10.1038/s41597-024-04029-x)
781 [04029-x](https://doi.org/10.1038/s41597-024-04029-x), 2024.

782 Zhang, L., Xu, Y., Meng, C., Li, X., Liu, H., and Wang, C.: Comparison of Statistical and Dynamic
783 Downscaling Techniques in Generating High-Resolution Temperatures in China from CMIP5
784 GCMs, *J. Appl. Meteorol. Climatol.*, 59, 207–235, <https://doi.org/10.1175/jamc-d-19-0048.1>,
785 2020.

786 Zhang, N., Gao, Z., Wang, X., and Chen, Y.: Modeling the impact of urbanization on the local and
787 regional climate in Yangtze River Delta, China, *Theor. Appl. Climatol.*, 102, 331–342,
788 <https://doi.org/10.1007/s00704-010-0263-1>, 2010.

789 Zhang, S. and Li, X.: Future projections of offshore wind energy resources in China using CMIP6
790 simulations and a deep learning-based downscaling method, *Energy*, 217, 119321,
791 <https://doi.org/10.1016/j.energy.2020.119321>, 2021.

792 Zhang, Z. and Liu, Y.-A.: A 1 km Hourly High-Resolution 3D Wind Field Dataset over the Yangtze
793 River Delta during June-August 2021-2023, Science Data Bank [data set],
794 <https://doi.org/10.57760/sciencedb.23752>, 2025.

795